Supplementary Information

Room-Temperature Upcycling of Mixed PVC and Polyolefin Waste

Wei Zhang,[1,2+] Boda Yang,[1+] Benjamin A. Jackson,[1] Junbo Zhao,[2] Donald M. Camaioni,[1] Sungmin Kim,[1] Huamin Wang,[1] János Szanyi,[1] Jingguang G. Chen,[3] Mal-Soon Lee,[1]* and Johannes A. Lercher[1,2]*

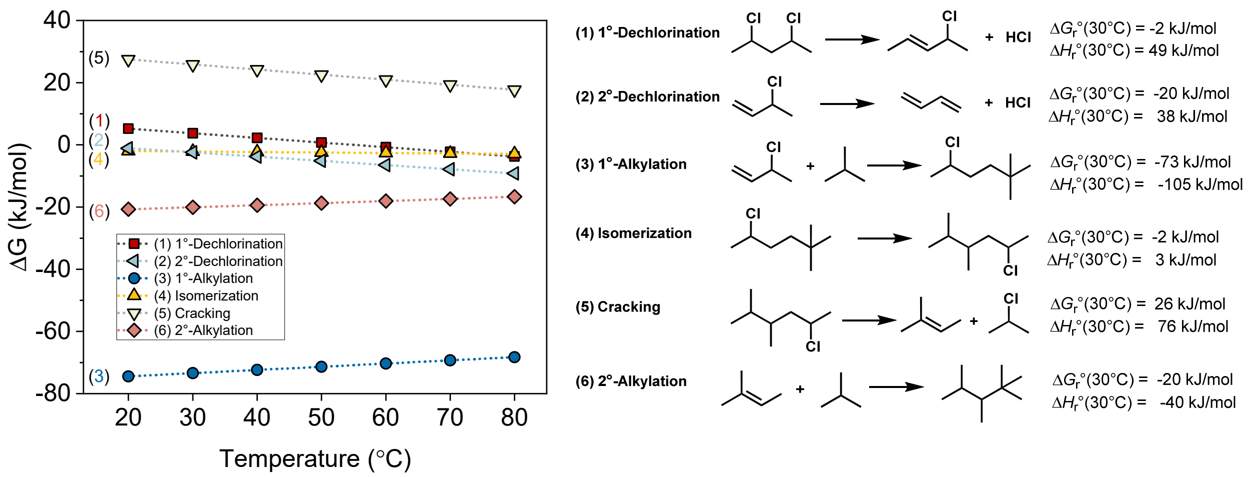

Extended Data Fig. 1 | Thermodynamic analysis of model reactions for dehydrochlorination, C-C bond cleavage, isomerization, and alkylation with the respective Gibbs free energy of reaction at varying temperatures and enthalpy changes using HSC chemistry 10 software at the indicated temperatures.

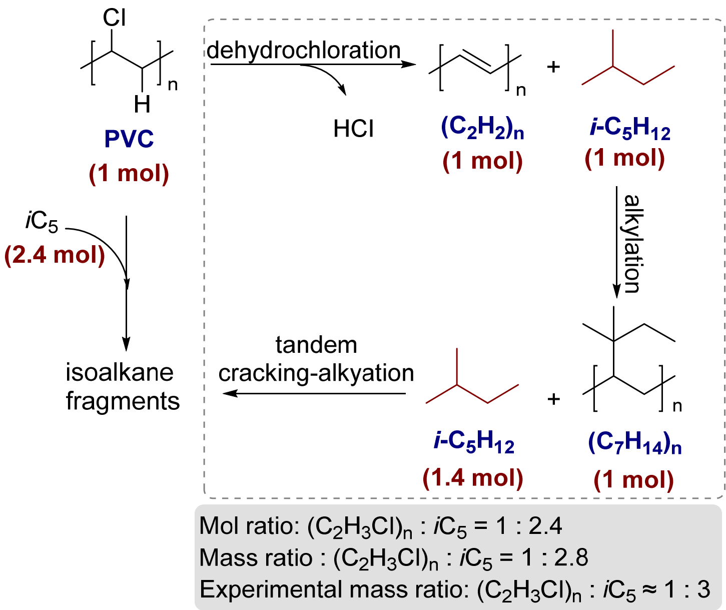

Extended Data Fig. 2 | Stoichiometry ratio between PVC and i-C_5 in the tandem dechlorination-alkylation-cracking reaction.

The presented mechanism demonstrates that PVC undergoes a dehydrochlorination reaction, leading to the formation of C=C double bonds (Fig. 3 in main text). It further undergoes alkylation with iC_5, resulting in the saturation of the polymer chain. This process is comparable to the cracking of polyolefins. During the dehydrochlorination-alkylation step, the stoichiometric molar ratio between the PVC monomer and *i*C_5 is 1:1. Our recent study showed that the stoichiometric mass ratio of polyolefin/iC_5 was 1:1 (Science 2023, 379, 807–811). Given that the carbon number of the polymer chain increases by 1.4 times due to the initial alkylation, the overall stoichiometric mole ratio between the PVC monomer and i-C_5 adjusts to 1:2.4. This ratio translates to approximately 1:2.8 in mass ratio in an ideal condition, assuming no production of aromatic or unsaturated hydrocarbons.

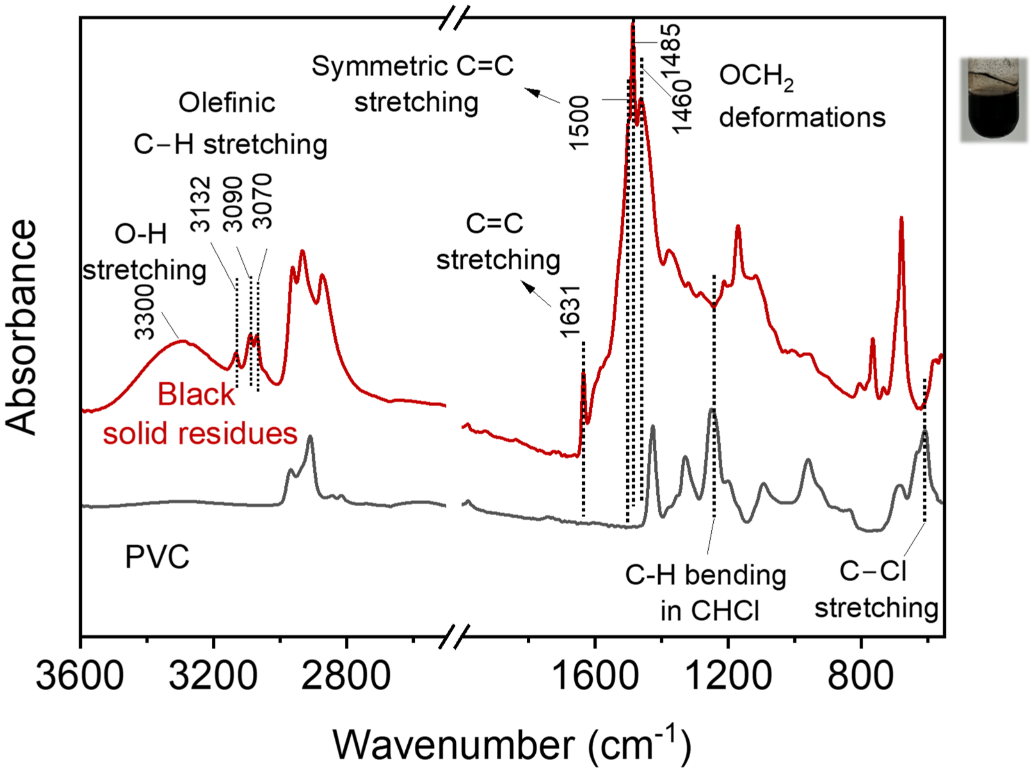

Extended Data Fig. 3 | ATR-FTIR spectra of black solid residues from PVC dehydrochlorination without iC_5 as co-reactant.

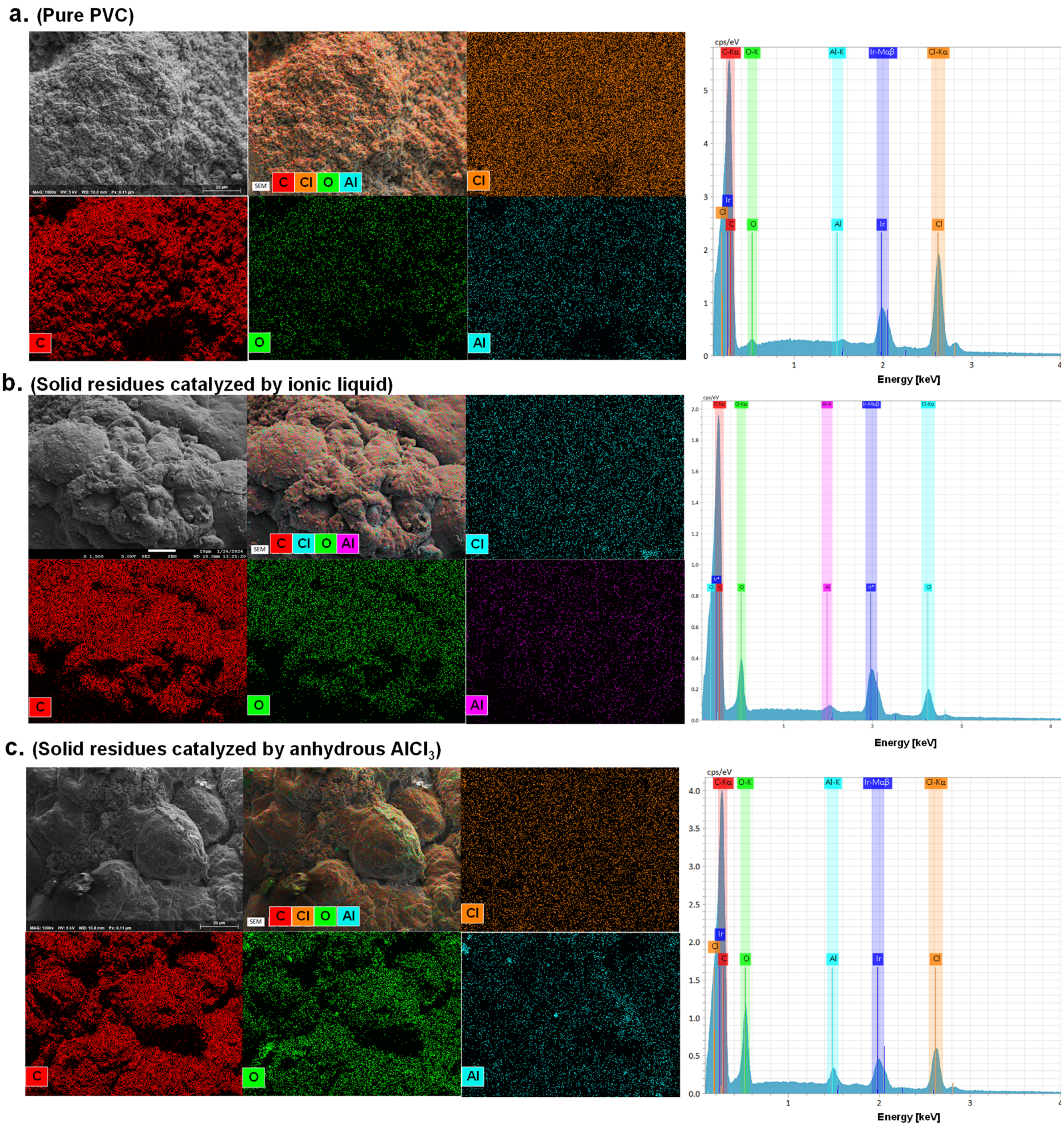

Extended Data Fig. 4 | Representative SEM image, corresponding elemental mapping and energy dispersive X-ray (EDX) analysis of PVC before and after reaction. (**a**) pure PVC; (**b**) black solid residues in $C_4PyCl\text{-}2AlCl_3$ catalyzed PVC dechlorination (in the absence of iC_5); (**c**) black solid residues in anhydrous $AlCl_3$ catalyzed PVC dechlorination (in the absence of iC_5).

Extended Data Table 1| Summary of elemental (CHNS) analysis, atomic ratios calculated from the energy dispersive X-ray (EDX) analysis of PVC before and after reaction (in the absence of iC_5).

Samples	CHNS analysis			EDX analysis					Average atomic ratio	
	C (wt. %)	**H** (wt. %)	**100-[(C + H)]** (wt.%) [a]	**C** (wt. %)	**Cl** (wt. %)	**O** (wt.%)	**Al** (wt.%)	**[Cl + O]** (wt. %)[b]	**C/ H/ Cl**	**C/ H/ (Cl +O)**
PVC	38.5	4.3	57.2	45.1	53.5	1.4	0	54.9	1 /1.3 /0.5	1 /1.3 /0.5
Solid residues ($C_4PyCl-2AlCl_3$)	62.9	5.9	31.2	59.8	22.7	16.6	0.9	32.3	1 /1.1 /0.1	1 /1.1 /0. 3
Solid residues (anhydrous $AlCl_3$)	49.8	3.2	47.0	47.6	33.5	16.2	2.7	49.7	1/ 0.8 / 0.2	1 /0.8 /0.5

[a] Values obtained from CHN analysis; [b] Values obtained from EDX analysis

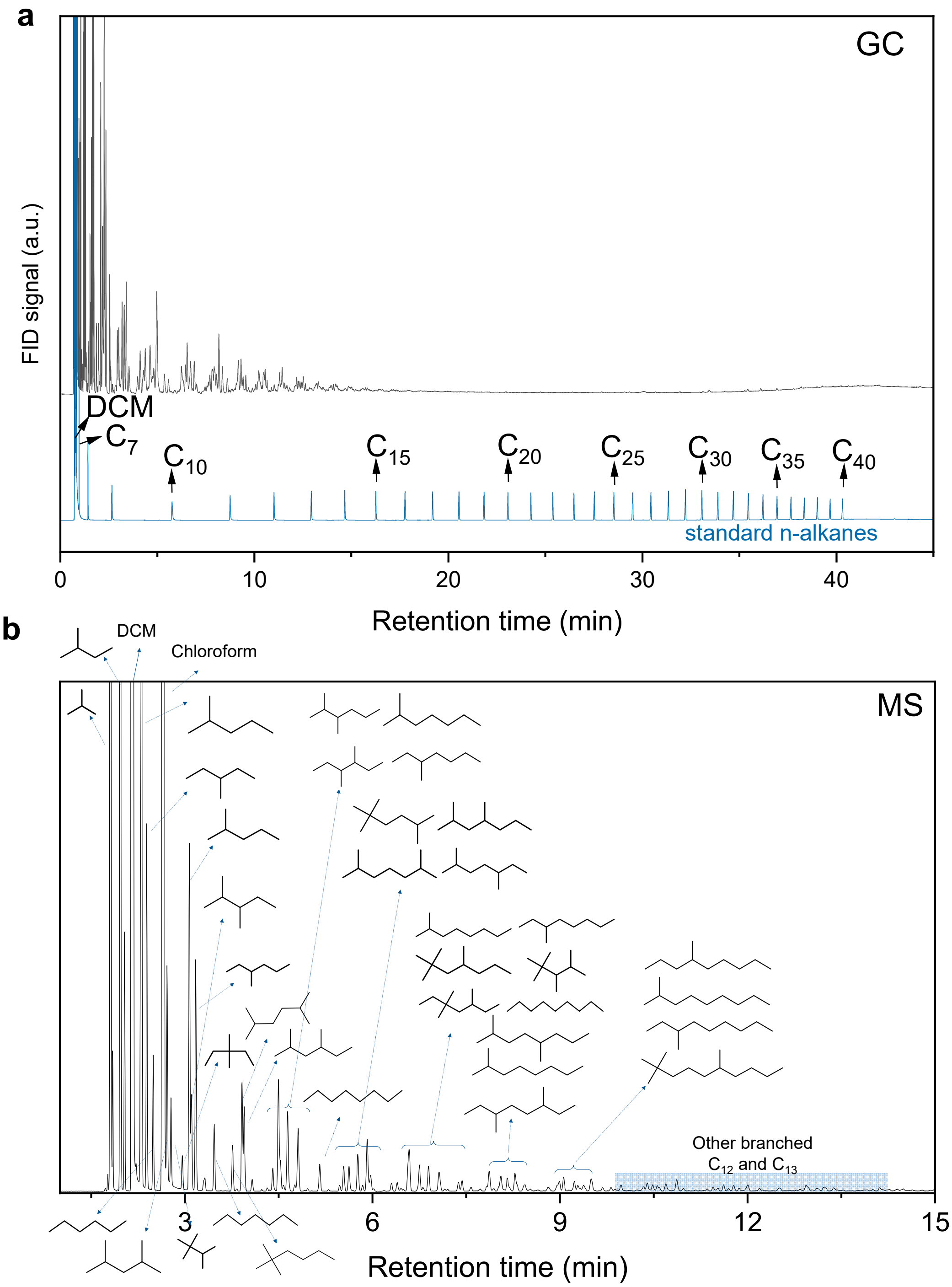

Extended Data Fig. 5 | GC and MS analysis of hydrocarbon products (≥C_4) from the organic layer of PVC-iC_5 upcycling over $AlCl_3$-based chloroaluminate ionic liquid (C_4PyCl-2$AlCl_3$), using n-alkanes as the reference standard. The main products are mainly cantered on the range of C_4-C_{10} and negligible heavy alkanes (C_{12}-C_{40}).

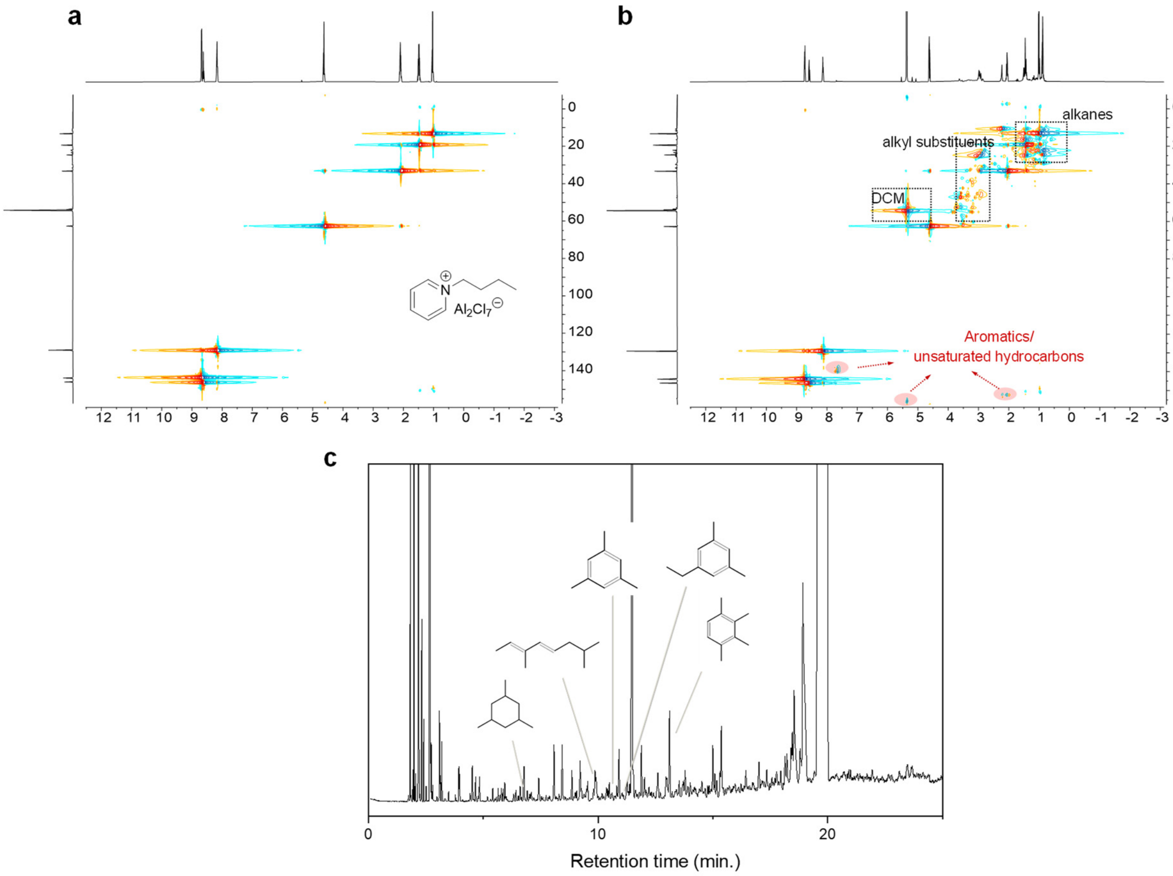

Extended Data Fig. 6 | 2D ^{1}H-^{13}C COSY NMR spectra of the pure ionic liquid (**a**) and the bottom ionic liquid layer post-reaction (**b**), alongside GC-MS analysis of reaction products from the bottom layer (**c**).

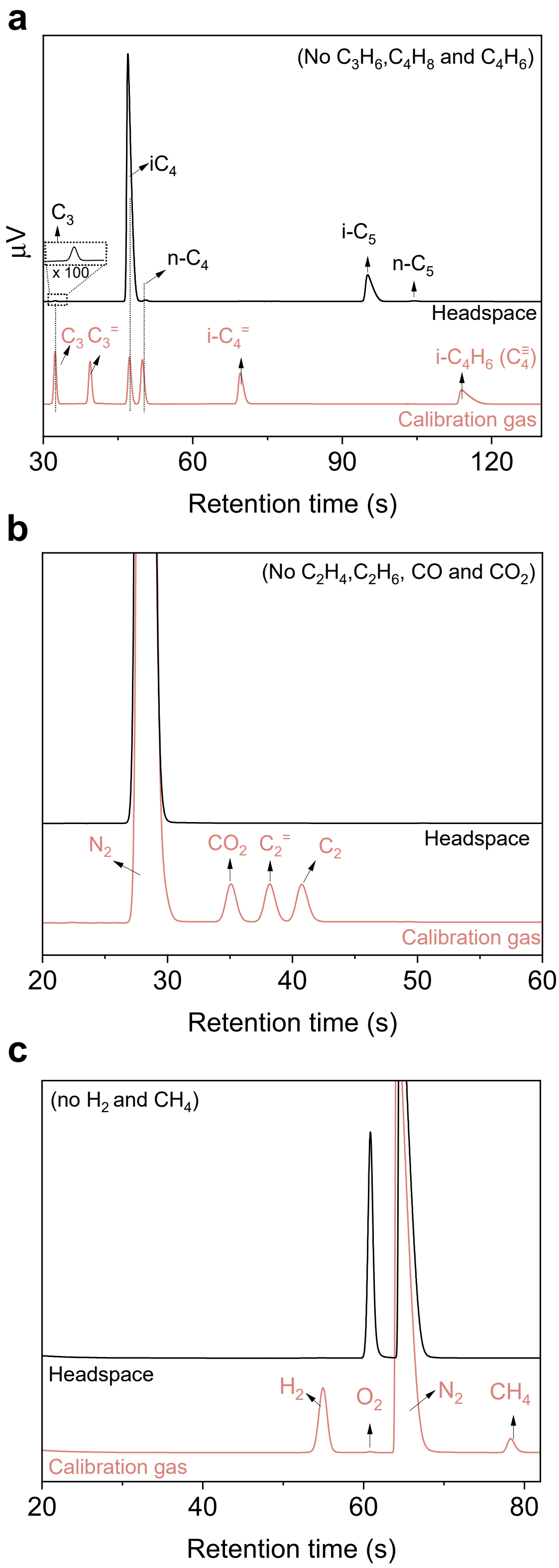

Extended Data Fig. 7 | GC analysis of the headspace from the tandem catalytic PVC/iC_5 upcycling. Note that the gas compositions were analyzed using a micro gas chromatograph (INFICON, Micro GC Fusion®) equipped with three columns: (**a**)Rt®-Alumina BOND/Na_2SO_4, (**b**) Rxi®-1 ms and (**c**) Rt®-Q-Bond. Note that the micro-GC was calibrated using a standard calibration gas mixture, which included N_2, H_2, carbon monoxide (CO), carbon dioxide (CO_2), methane (CH_4), ethane (C_2), ethylene($C_2^=$), propane (C_3), propylene ($C_3^=$), isobutane (iC_4), n-butane (nC_4), and n-butene (n$C_4^=$).

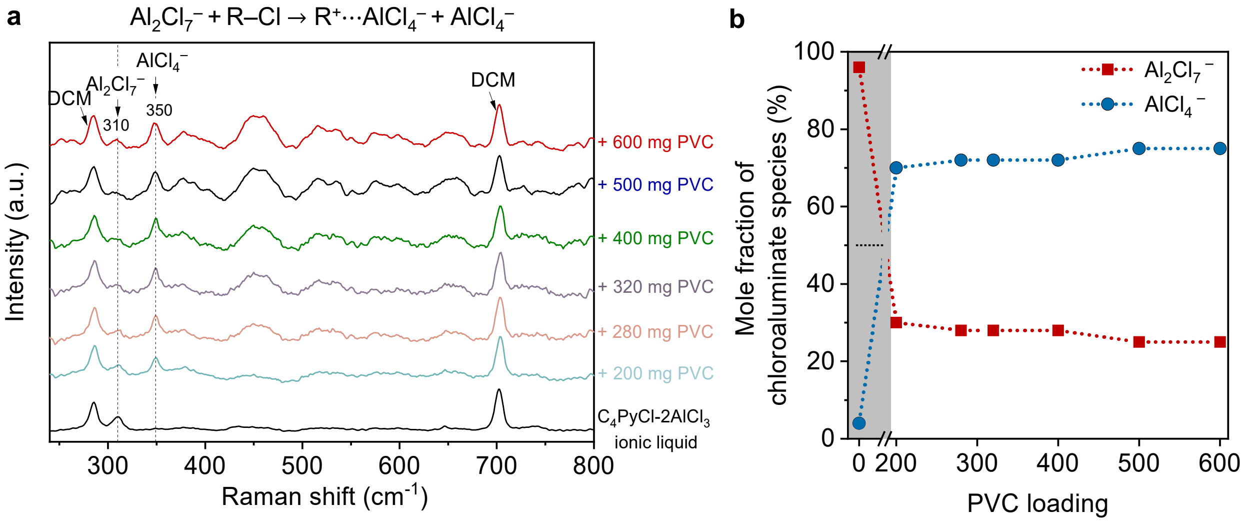

Extended Data Fig. 8 | a, Raman spectra of chloroaluminate ionic liquid (C_4PyCl-$2AlCl_3$) varying different PVC loading recorded after the PVC-iC_5 reaction. **b**, the corresponding variation of chloroaluminate species of $Al_2Cl_7^-$ and $AlCl_4^-$. Note that the area ratio of Raman signals at 310 cm^{-1} and 350 cm^{-1} depends closely on the molar ratio $Al_2Cl_7^-$ to $AlCl_4^-$. The Raman spectra of the C_4PyCl-$2AlCl_3$ ionic liquids showed a characteristic peak at 310 cm^{-1}, which is attributed to the symmetric Al–Cl–Al stretching of dimeric $Al_2Cl_7^-$ anions. PVC reacts with $Al_2Cl_7^-$ during dehydrochlorination to generate PVC-derived carbenium ions and $AlCl_4^-$ ion pairs, with additional $AlCl_4^-$ acting as counterions ($Al_2Cl_7^- + R$-$Cl \rightarrow R^+\cdots AlCl_4^- + AlCl_4^-$). Therefore, adding PVC results in the characteristic $AlCl_4^-$ peak at 350 cm^{-1}, attributed to symmetric Cl−Al−Cl stretch of $AlCl_4^-$.

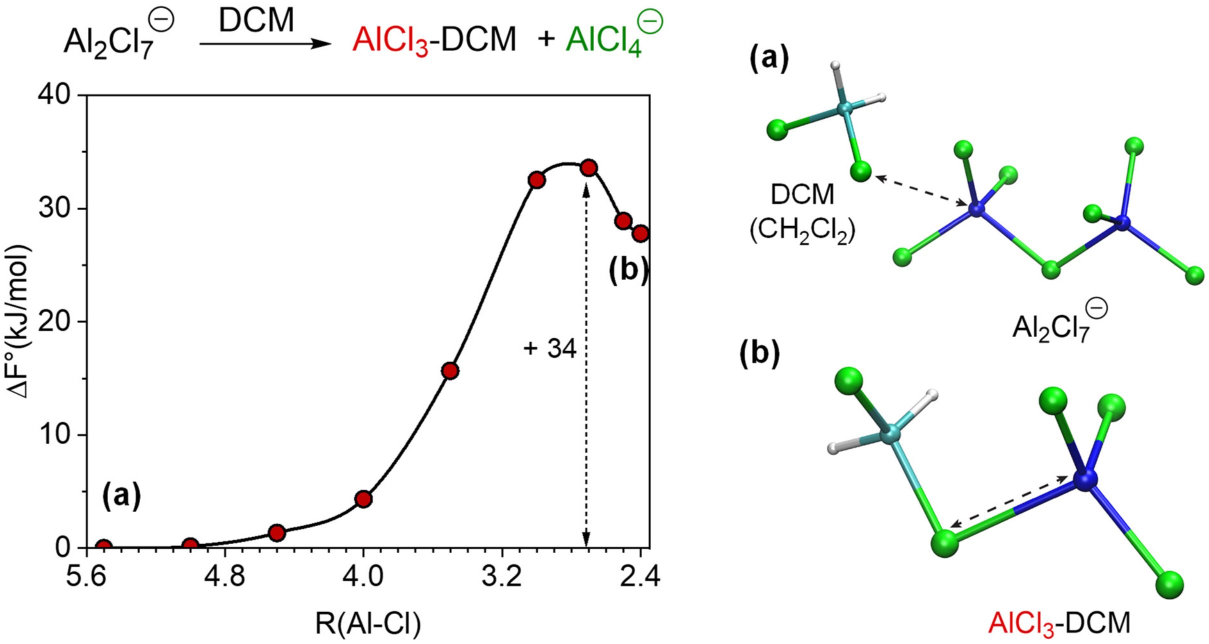

Extended Data Fig. 9 | Computed reaction pathway for the dissociation of $Al_2Cl_7^-$. The standard Helmholtz free energy (ΔF°) as a function of the internuclear distance of Al-Cl for the reaction of DCM and Al_2Cl_7 to form $AlCl_4^-$ and a $AlCl_3$-DCM adduct. Note that ΔF° is calculated using the Blue Moon ensemble approach for ab initio molecular dynamics trajectories. Included are representative structures along the reaction pathway; a black dotted line is added to the structures to indicate the internuclear distance constrained in the Blue Moon calculations.

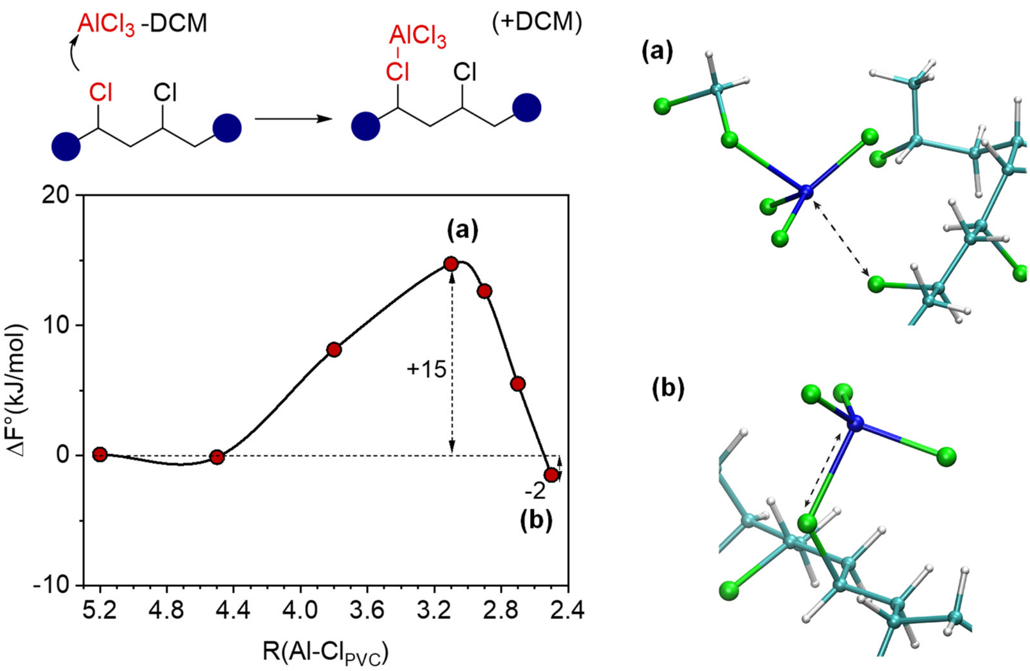

Extended Data Fig. 10 | Computed reaction pathway for the chloride transfer from Cl_{PVC} to the $AlCl_3$-DCM adduct. The standard Helmholtz free energy (ΔF°) as a function of the internuclear distance of Al-Cl for the reaction between the $AlCl_3$-DCM adduct and PVC. Note that ΔF° is calculated using the Blue Moon ensemble approach for ab initio molecular dynamics. Included are representative structures along the reaction pathway; a black dotted line is added to the structures to indicate the internuclear distance constrained in the Blue Moon calculations.

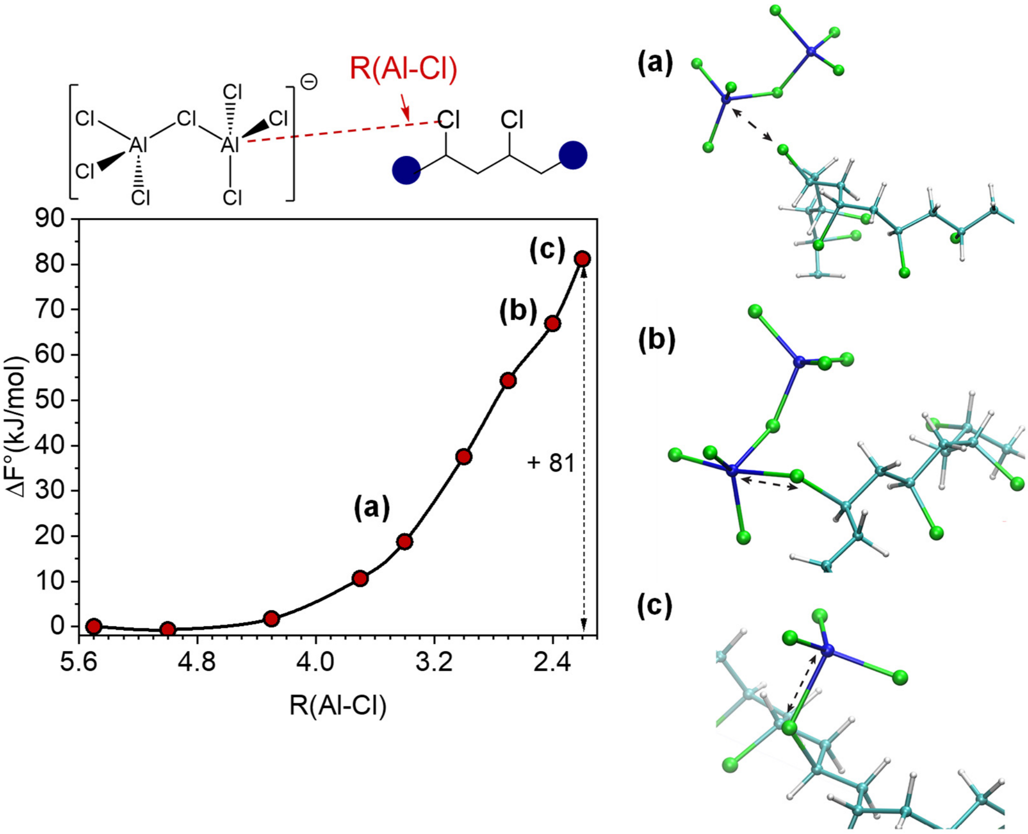

Extended Data Fig. 11 | Computed reaction pathway for the chloride transfer from Cl_{PVC} to $Al_2Cl_7^-$. The standard Helmholtz free energy (ΔF°) as a function of the internuclear distance of Al-Cl for the reaction between $Al_2Cl_7^-$ and PVC. Note that ΔF° is calculated using the Blue Moon ensemble approach for ab initio molecular dynamics. Included are representative structures along the reaction pathway; a black dotted line is added to the structures to indicate the internuclear distance constrained in the Blue Moon calculations.

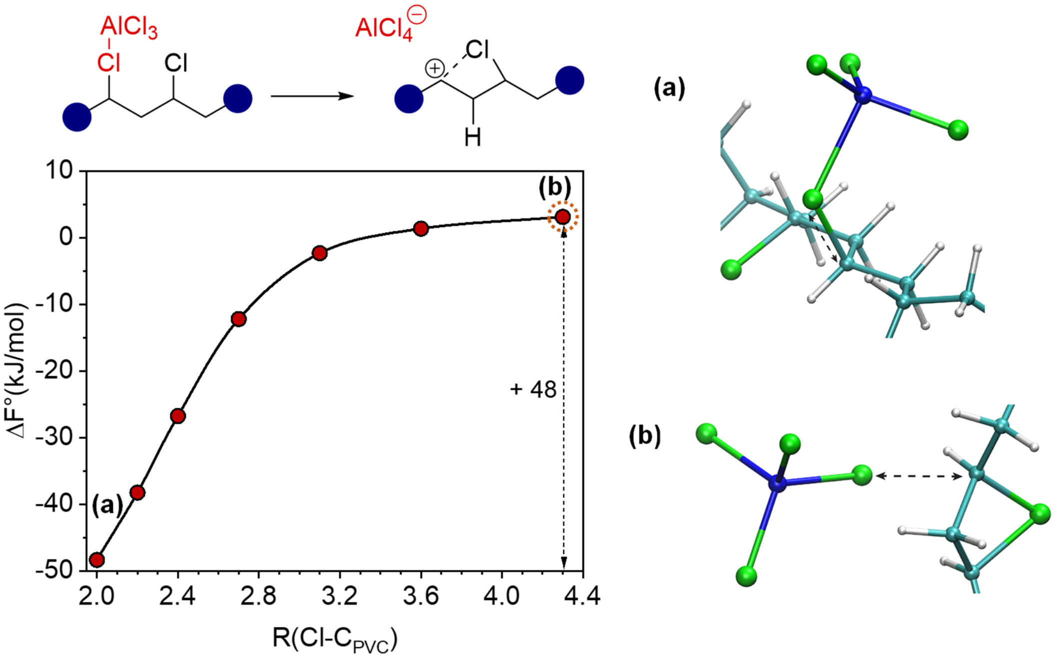

Extended Data Fig. 12 | Computed reaction pathway for the dissociation of $AlCl_4^-$. Plotted is the standard Helmholtz free energy (ΔF°) as a function of the internuclear distance of Cl-C_{PVC} for the dissociation of $AlCl_3$ and the coordinated PVC Cl to form $AlCl_4^-$ and a carbonium ion in the PVC chain. The carbonium ion is immediately stabilized by an adjacent PVC Cl to form a halonium ion (**b**). Note that ΔF° is calculated using the Blue Moon ensemble approach for ab initio molecular dynamics trajectories. Included are representative structures along the reaction pathway; a black dotted line is added to the structures to indicate the internuclear distance constrained in the Blue Moon calculations.

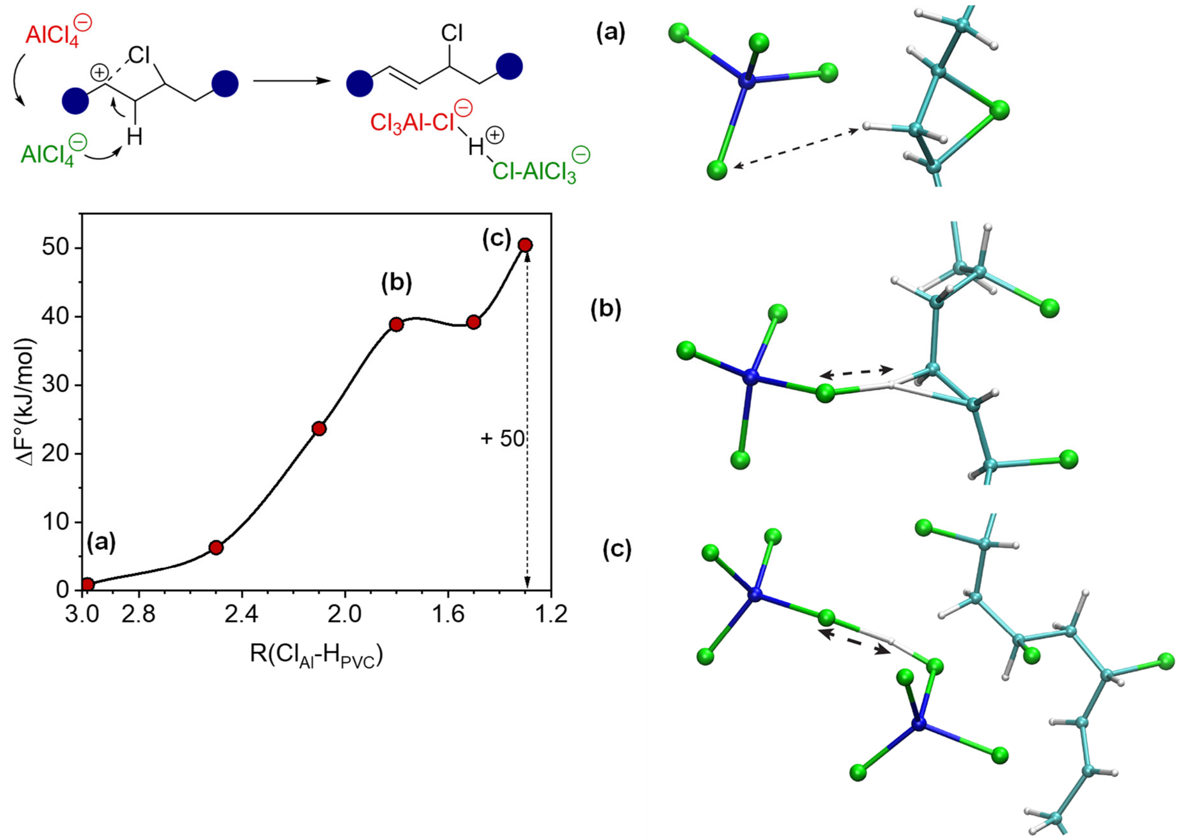

Extended Data Fig. 13 | Computed reaction pathway for the deprotonation of PVC by $AlCl_4^-$. Plotted is the standard Helmholtz free energy (ΔF°) as a function of the internuclear distance of Al-H for the deprotonation by $AlCl_4^-$ of a partially dechlorinated PVC to form a C=C bond. During the trajectory, a second nearby $AlCl_4^-$ rapidly moves in to coordinate $AlCl_4H$ sharing the H+ between the two and forming $AlCl_4^-{-}H^+{-}AlCl_4^-$ (**a**), a relatively stable, transient species which may recombine to form Al_2Cl_7 and HCl. Note that ΔF° is calculated using the Blue Moon ensemble approach for ab initio molecular dynamics trajectories. Included are representative structures along the reaction pathway; a black dotted line is added to the structures to indicate the internuclear distance constrained in the Blue Moon calculations.

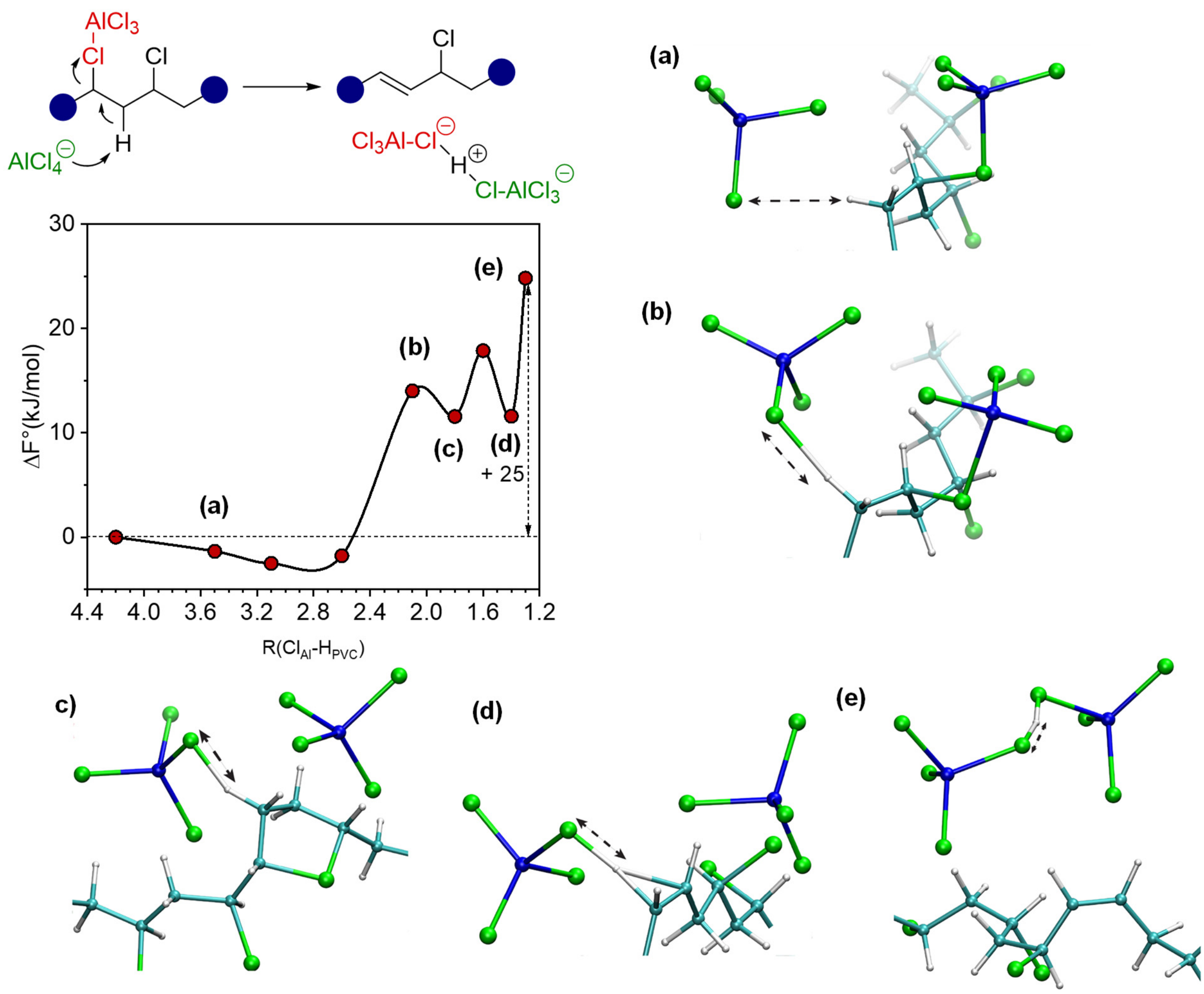

Extended Data Fig. 14 | Computed reaction pathway for the dehydrohalogenation of PVC by $AlCl_4^-$. Plotted is the standard Helmholtz free energy (ΔF°) as a function of the internuclear distance of Al-H for simultaneous deprotonation of PVC by $AlCl_4^-$ and its dechlorination by $AlCl_3$ to form a C=C bond in PVC and the $AlCl_4^-$−H^+−$AlCl_4^-$ intermediate. The stabilization of the carbonium ion by the still coordinated $AlCl_4^-$ halves the reaction barrier. Note that ΔF° is calculated using the Blue Moon ensemble approach for ab initio molecular dynamics trajectories. Included are representative structures along the reaction pathway; a black dotted line is added to the structures to indicate the internuclear distance constrained in the Blue Moon calculations.

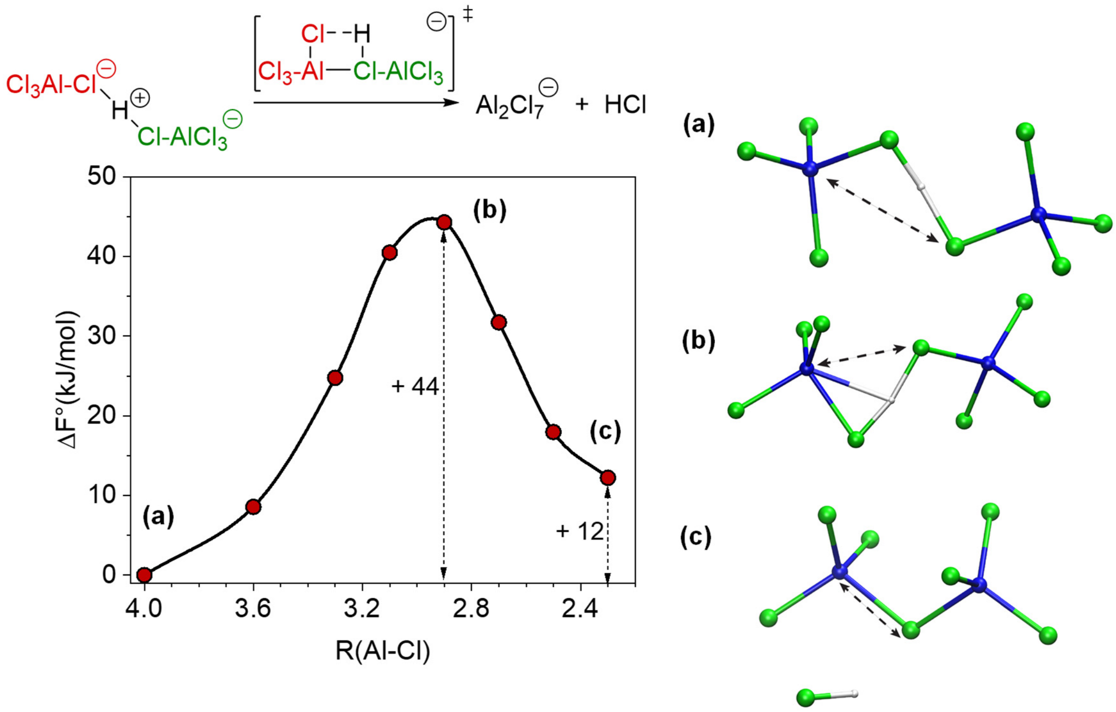

Extended Data Fig. 15 | Computed reaction pathway for the dehydrohalogenation of $AlCl_4^-{-}H^+{-}AlCl_4^-$ intermediate to form $Al_2Cl_7^-$ and HCl. Plotted is the standard Helmholtz free energy (ΔF°) as a function of the internuclear distance of Al-Cl for the recombination of $AlCl_4^-{-}H^+{-}AlCl_4^-$ to form $Al_2Cl_7^-$ and HCl. Note that ΔF is calculated using the Blue Moon ensemble approach for ab initio molecular dynamics trajectories. Included are representative structures along the reaction pathway; a black dotted line is added to the structures to indicate the internuclear distance constrained in the Blue Moon calculations.

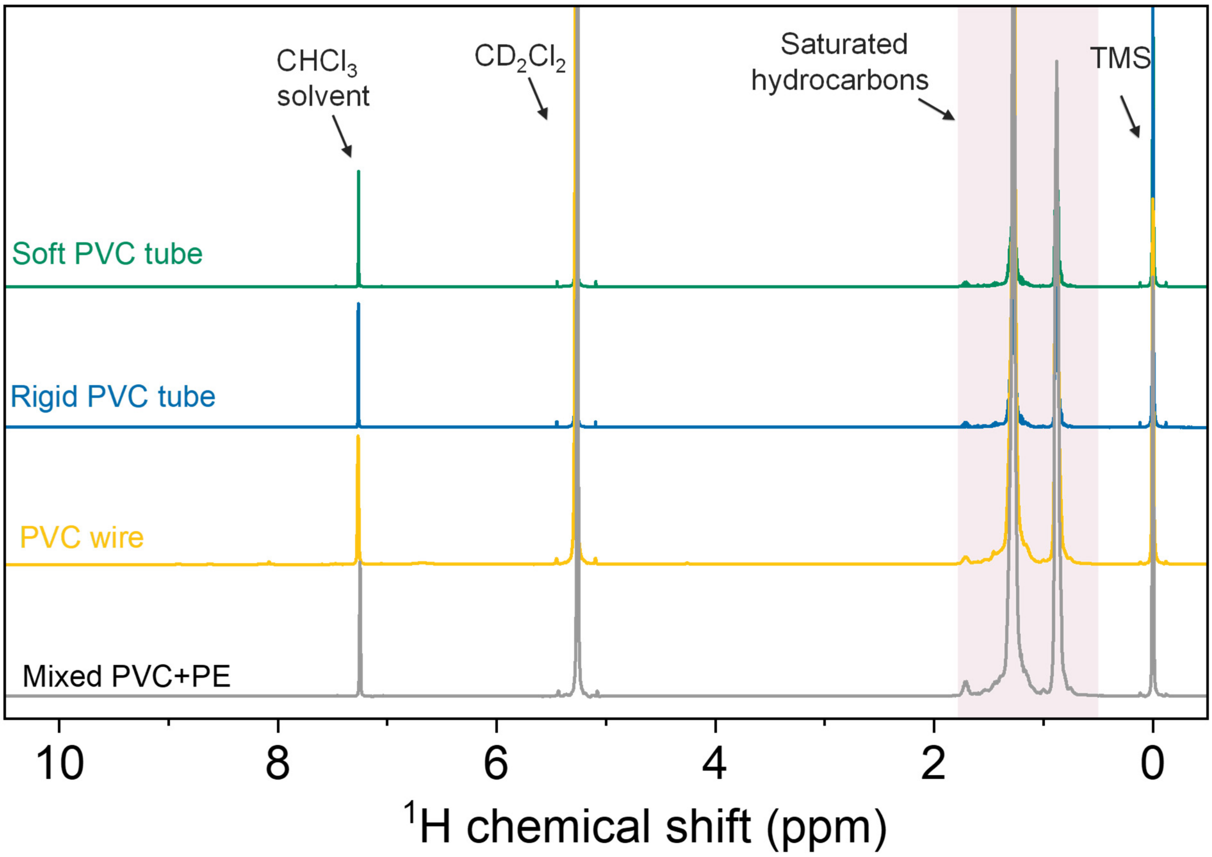

Extended Data Fig. 16 | ^{1}H NMR spectra of products in the upper organic layer after the transformation of post-consumer polyolefin waste with *i*C_5 over C_4PyCl-2AlCl_3.